33rd EUROPEAN ROTORCRAFT FORUM

Kazan, Russia - September 11-13, 2007

Conditional Averaging Methodology for Periodic Data with Time Jitter and Spatial Scatter

Berend G. van der Wall, Oliver Schneider
DLR, Inst. of Flight Systems, Braunschweig, Germany

The conditional averaging methodology is shown to be mandatory to proper average essentially periodic data that are biased by spatial scatter and time jitter effects which are always present in both flight and wind tunnel test. This is demonstrated at various data of completely different physical origin as obtained from the Higher Harmonic Control Aeroacoustic Rotor Test (HART II) performed in the Large Low-Speed Facility (LLF) of the German/Dutch Wind Tunnel (DNW): blade position and tip vortex flow field data (both obtained instantaneously and with optical measurement techniques), blade surface pressure and acoustic data (measured continuously by absolute pressure transducers and microphones, respectively).

1 Introduction

In helicopter rotor experimental data - either originating from the flying helicopter or from the wind tunnel model - periodic and non-periodic motions of the test vehicle are present due to gusts and transient motion of the helicopter or due to flexibility of model support and unsteadiness in the wind tunnel environment. These motions usually are of low-frequency nature compared to the rotor rotational frequency, but they slightly change the aerodynamic environment revolution by revolution. Consequently the data like rotor blade position, blade pressure, vortex position, microphone pressure exhibit disturbances in space and/or time that must properly be addressed in data analysis, especially when the time (or space) averaged data are to be computed. These averaged data (velocity fields, position or pressure time histories) are the basis for code validation efforts and thus special algorithms must be applied to eliminate these spatial scatter and/or time jitter effects appropriately.

The most frequently used method of averaging is the so-called simple (= arithmetic) averaging. Provided that a number of periods N_p (one period = one rotor revolution) have been recorded for each sensor - favorably with a constant number of samples N_s per period and additionally each sample y_i at the same phase location ψ_i within each period (which is usually the case in rotary wing data that are triggered to the main rotor azimuth ψ with 1/rev as the dominating frequency) -, such an algorithm to compute an average sample $\bar{y}_i(j),\ i = 1, 2, ..., N_s$ of a time history reads in a generalized form

$$\bar{y}_i = \sqrt[m]{\frac{1}{N_p}\sum_{j=1}^{N_p} y_i^m(j)} \qquad i = 1, 2, ..., N_s \tag{1}$$

with

$m = -1$	harmonic average
$m \to 0$	geometric average
$m = 1$	simple (arithmetic) average
$m = 2$	quadratic average (or effective value)

and

$$y_{i,min} \le \bar{y}_i(m = -1) \le \bar{y}_i(m \to 0) \le \bar{y}_i(m = 1) \le \bar{y}_i(m = 2) \le y_{i,max}$$

The simple average ($m = 1$) is widely used in statistical analysis of variations in the individual samples and eliminates noise in a proper manner in order to obtain a smooth time-averaged history. The harmonic average is often used for data that contain a reference to a unit like velocities $m/s,\ km/h$ or densities

like mass/volume. In cases like proportionalities or growth rates, where instead of the sum the product of the samples is to be interpreted, the geometric average $m \to 0$ is often used, that is

$$\bar{y}_i = \sqrt[N_p]{\prod_{j=1}^{N_p} y_i(j)} \qquad i = 1, 2, ..., N_s \tag{2}$$

Another important parameter to judge the individual samples confidence in the relation to the average value is to make use of the standard deviation, which is defined as

$$\sigma_i = \sqrt{\frac{1}{N_p - 1} \sum_{j=1}^{N_p} \left(y_i(j) - \bar{y}_i\right)^2} \qquad i = 1, 2, ..., N_s \tag{3}$$

In a Gaussian normal distribution, which is expected in most cases, about 68% of all samples are within the range of $\bar{y}_i \pm \sigma_i$, about 95% within $\bar{y}_i \pm 2\sigma_i$, and about 99.8% within $\bar{y}_i \pm 3\sigma_i$.

In case the data are contaminated by spurious elements being either by far too large and/or too small compared to the majority of samples another procedure should be applied first by eliminating the same fraction of N_p at both ends of the scale before applying one of the averaging methods mentioned before. This is called the truncated average, but the truncation threshold (usually 5 to 15%) must be adapted manually to the individual distribution of data and thus requires some degree of experience in order to distinguish betweeen those data being obviously erroneous and those that should be retained. Often a value between 2σ and 3σ is used as a threshold to identify those samples as outliers. However, the mathematical formulation requires truncation at both ends of the scale with the same number of samples, which in some cases does not match the physics of the data. Some other higher order variants of the truncated average exist that use weighing functions.

As an example for instantaneous data that are not available in time rather than in space the result of flow field measurements like PIV can be seen. Herein neighboring data (velocity vectors) are space-correlated. The preprocessing of particle images to velocity vectors usually leads to some spurious vectors that must be eliminated before analysing the velocity vector field. Their identification is based on statistical analysis of a certain subset of vectors around that one in question. Once identified as spurious, these vectors normally are of significantly larger magnitude and different orientation (although the orientation alone cannot be used as indicator, for example the orientation naturally changes to the opposite when passing the center of a vortex) than those vectors computed correctly, but rarely of significantly smaller length. Thus, clipping the same number of vectors at both ends of the length scale would eliminate a lot of correct samples at the lower end and appears not appropriate to the problem.

Another example is given with continuous data as obtained from strain gauges, pressure sensors or microphones. Within each sensor time history the individual samples are time-correlated to form a continuous curve. Any spikes - like those caused by slip-ring problems or broken cables - can easily be detected either by correlation to the neighboring samples within an individual time history, or by correlation with the samples at the same phase of the rest of the periods measured. However, in case this is a repetetive problem occuring in each period relying on the latter method alone would not work. A space-correlation must also exist to continuous data obtained from another sensor located close enough, such that this information could also be used to identify spurious data, but care must be taken since this often includes non-linear phase shifts between the time histories.

So far, the averaging methods mentioned are mainly useful when statistically distributed, mainly one-dimensional, data are to be averaged and no other information about the physics behind has to be obeyed. Yet, a fundamental problem cannot be addressed by those averaging methods, and this is the spatial scatter of individual events of interest. Applying any of the averaging methods mentioned would result in artificially smoothing the individual events which makes an analysis of these obsolete. To illustrate the problem see Fig. 1.

As can be seen in this example, in each individual time history an identical event is seen and the final goal is to provide an averaged time history as indicated by CA = conditionally average. The line denoted SA represents the result of simple averaging using Eq. 1 with $m = 1$ and it is clearly visible that the individual characteristics are widely lost. In case this was a measurement of the induced velocities of a vortex when passing the probe each individual analysis would lead to correct core radius and swirl velocity, but the averaged time history would give completely wrong results for both parameters despite a correct average position of the event. The reason is the time jitter of the event that leads to artificial smoothing. In contrast, the conditional average provides both correct position and retains all information

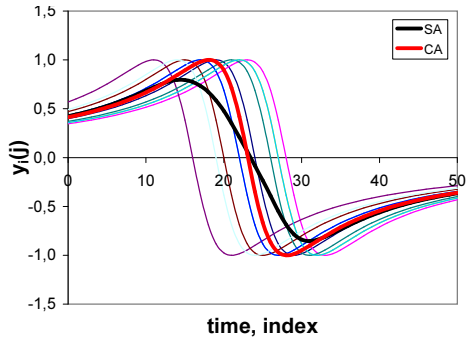

Figure 1: Effect of time jitter on averaged time history (SA - simple average; CA - conditional average).

of the individual time history. To circumvent the time jitter effect, two possible solutions have been elaborated and used in the past:

1. in the space-time domain: to identify the parameters of the event in each individual measurement and then apply one of the averaging methods to the parameters identifies. However, the individual analysis often is biased or hindered by noise and the result is a set of parameters, but no averaged time history or spatial distribution of data is available.

2. in the frequency domain: for each individual period of the time history the Fourier spectrum is computed, then all spectra are averaged. This is appropriate for the magnitudes of the spectrum, but the time information (= phase) gets lost and again no averaged time history is available.

The effect of time jitter on the results of the spectrum and corrections to it in the frequency domain were elaborated, for example by [5]. In this article an alternative method is presented known as the conditionally averaging that takes into account spatial scatter and time jitter and as a result provides averaged spatial distributions or time histories that eliminate noise but still include all the information of the individual event. In time history data, the goal is to generate averaged time histories that have a Fourier spectrum similar to the averaged spectrum.

2 The HART II data base

All the analysis methodologies are applied to the HART II test data obtained 2001 in the DNW by DLR, ONERA, NASA Langley, US Army AFDD and DNW. These data encompass measurements of wind tunnel data, rotor balance, blade motion, blade pressure, acoustic radiation and detailed tip vortex flow field data. The HART II test is described in [1] and details of the test set-up and of the measurement techniques applied are given in [2]. Representative results applying part of the techniques described in this paper are shown in [3]. These reports and part of the data are available for the rotorcraft community within the framework of the international HART II workshop held semi-annually at both the AHS Forum and the European Rotorcraft Forum [4], sponsored by the HART II team.

Within HART II a Mach-scaled and dynamically scaled Bo105 model rotor with $N_b = 4$ rectangular blades at a pre-cone of $\beta_p = 2.5deg$, having a linear twist of $\Theta_{tw} = -8deg/R$, a radius of $R = 2m$, a chord of $c = 0.121m$ and a NACA23012 airfoil with trailing edge tab was operated in $6deg$ descent flight condition that is known to generate strong blade-vortex interaction (BVI) noise. The blade rotational speed was $\Omega = 109rad/s$ and the wind speed $V_\infty = 33m/s$, resulting in an advance ratio of $\mu = 0.151$. The thrust coefficient was set to $C_T = 0.0044$ representing a lightly loaded Bo105 and zero hub moments. The setup is shown in Fig. 2.

One of the main goals was to identify the physical mechanisms of higher harmonic control (HHC) on noise and vibration reduction by means of extensive flow field measurements. Three distinctive conditions were mainly investigated, these are the baseline case (referred to as BL) with a shaft angle of $\alpha_S = 5.3deg$ and zero roll and pitch moments. The application of HHC features two variants trimmed to the same condition as the BL case: the minimum noise case (MN) with 3/rev pitch control of $\Theta_3 = 0.8deg$ at the blade root at a phase of $\psi_3 = 300deg$, and the minimum vibration condition (MV) with the same pitch amplitude, but a different phase of $\psi_3 = 180deg$. These conditions were identified in the first HART test of 1994 [8].

Since the model rotor operated in 1994 was not available for HART II, another originally uninstrumented Bo105 model rotor was used where two blades were equipped with in total 51 absolute pressure transducers prior to the test. The leading edge differential pressure at 3% chord could thus be measured from 40-97% radius at 11 radial sections, and the chordwise pressure distribution at 87% radius could be recorded by means of 17 sensors as sketched in Fig. 2. By chordwise integration of these sensor signals the local lift time history in terms of the normal force coefficient $C_n M^2$ or local blade circulation $\Gamma_b = C_n V c/2$ with $V(\psi)$ as the time-varying air speed at the section can be evaluated. 80 successive rotor revolutions were recorded, triggered to the rotor azimuth at a data rate of 2048 samples/rev within each condition.

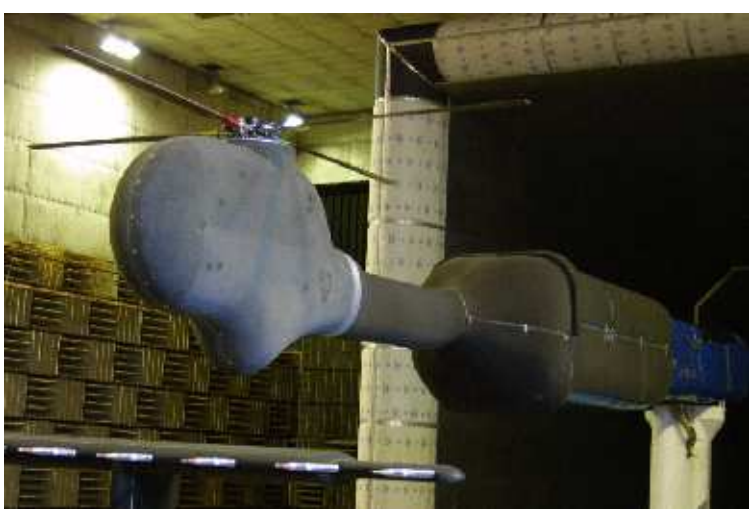

(a) Model rotor in the LLF of the DNW

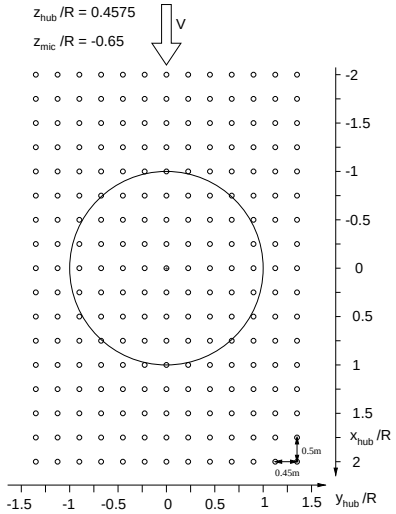

(b) Microphone measurement positions

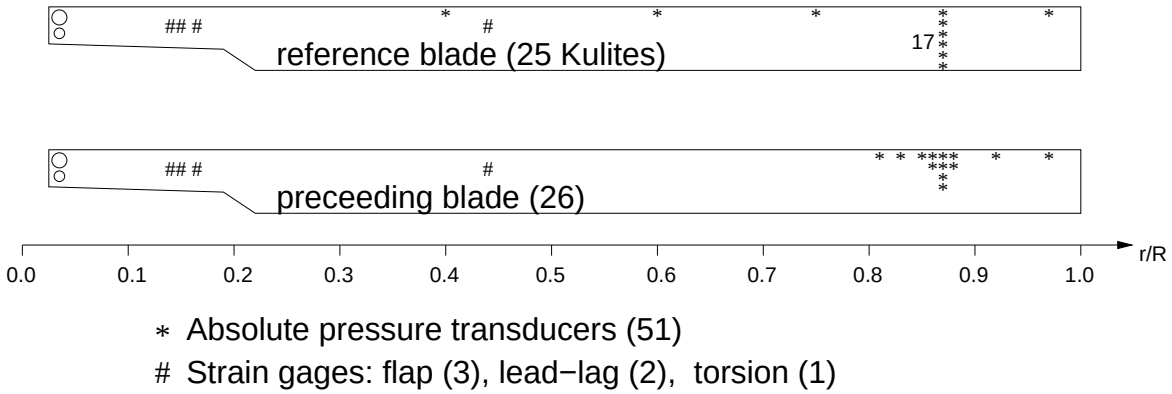

(c) Distribution of pressure sensors on the blades

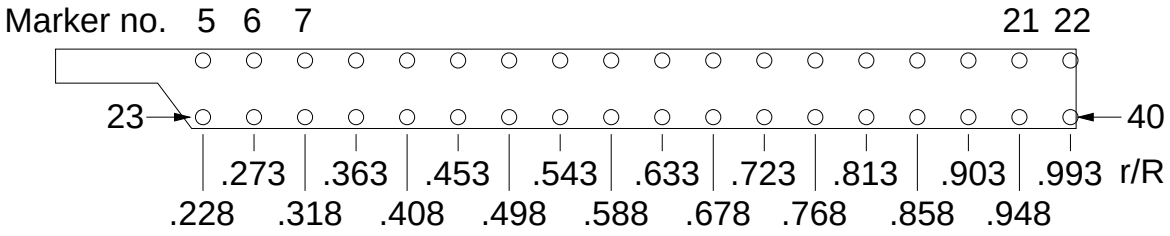

(d) Distribution of SPR markers on the blades

Figure 2: HART II equipment used for measurement of acoustics, blade pressures and blade deflection.

Acoustic pressure data were recorded $1.1075R$ below the rotor using an array with 13 microphones spaced equally at a distance of $0.225R$ that was traversed fore and aft of the rotor centre by a range of $\pm 2R$ at 17 downstream locations separated by $0.25R$, see Fig. 2. At each traverse location microphone data were recorded for 100 successive rotor revolutions at a data rate of 2048 samples/rev, again triggered to the rotor azimuth. The post-processing provides noise levels at every location based on spectral analysis of each individual revolution recorded. Putting together the result for all positions leads to the radiated

noise carpet as final output.

The blade position was measured optically using Stereo Pattern Recognition (SPR) [9]. Four cameras were mounted on the floor taking images of the rotor at 24 specified azimuthal locations equally distributed around the revolution. All four blades were equipped with 18 markers all along the leading edge as well as along the trailing edge as given in Fig. 2. The computation of the marker centers by means of image processing and a proper calibration resulted in the absolute position in space of these marker centers with an accuracy of $0.4mm$, which is 0.33% chord (or 0.02% radius). Since the cameras could not measure continuously rather than were limited by a maximum frequency of about $10Hz$, one image was recorded every $7th$ revolution and a minimum of 50 repeats was taken at every blade azimuth position to allow a statistical analysis.

The post-processing is described in detail in [6] and allows the identification of flap and lead-lag position of the quarter chord line along the span at each azimuth. Putting together all azimuthal positions in sequence the time history of blade motion can be computed by means of Fourier analysis and synthesis for intermediate azimuth locations. The elastic deformation is obtained subtracting the pre-cone rigid blade position. Differentiating the leading edge and trailing edge marker positions provides information about the radial distribution of the local pitch angle with an accuracy of $0.4deg$. When subtracting the build-in pre-twist and the commanded blade root pitch control the elastic torsion is obtained.

Flow field measurement were performed using Stereo Particle Image Velocimetry (SPIV od 3C-PIV) [10]. A large observation area of $0.45m * 0.37m$ was taken by DNW cameras for the global velocity distribution and global wake structure analysis and simultaneously a small observation area of $0.15m * 0.13m$ was gathered by DLR cameras for analysis of the blade tip vortex structures. The pre-processing of the camera images results in velocity vector fields, while the post-processing is devoted to analyse these vector maps first for the vortex spatial position, then for the vortex properties in order to identify parameters like the core radius r_c, the maximum swirl velocity at the core radius V_c and the swirl velocity profile $V_s(r)$. Other parameters like vortex circulation may be computed based on these results. The methods of post-processing are dexcribed in [7].

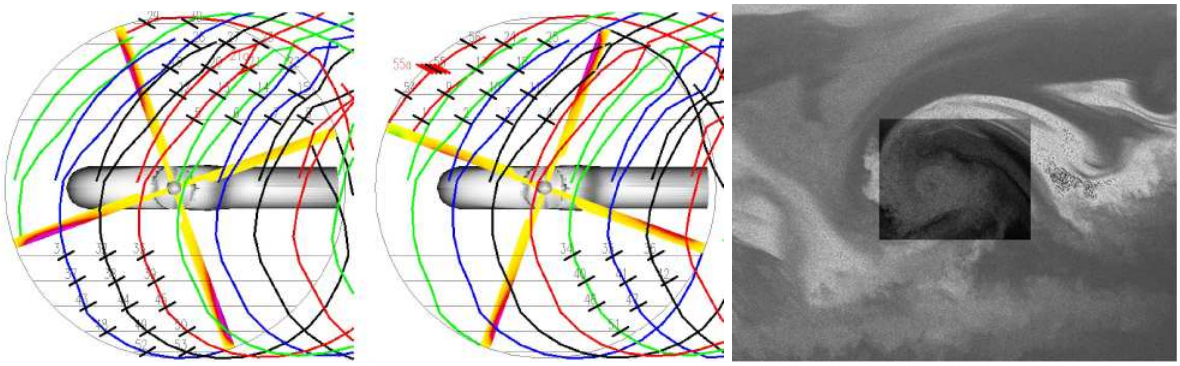

(a) PIV locations, MV

(b) Raw data PIV image, BL, Pos. 21, lower camera

Figure 3: PIV measurement positions and exemplary raw data images.

As in SPR measurements, the cameras were triggered to the rotor azimuth and recorded an image every $7th$ revolution, with 100 repeats. A traversing system allowed to cover the entire rotor disk outside $|y|/R = 0.4$ such that on either side of the rotor disk the tip vortices were traced from their creation at the trailing edge downstream until the rear end of the disk in lateral planes located at $y/R = \pm 0.4, +0.55, \pm 0.7, \pm 0.85, \pm 0.97$. The positions measured are indicated in Fig. 3 at the example of the MV case, where dual vortex systems exist over part of the revolution due to download at the blade tip itself. The right figure exemplarily shows a raw data image of the BL case at position 21 where the full size represents the large observation area and the inner image represents the small observation area with about three times the spatial resolution.

A secondary post-processing puts together the downstream measurements of the tip vortex which results in the vortex trajectory (and locations where the vortex passed the path of the blades), as well as the aging of the vortex by means of the development of its identified parameters like r_c or V_c. Some preliminary analysis was given in [3].

3 Body and blade motion

By means of stereo pattern recognition technique (SPR) the spatial position of markers attached to each of the four blades and to the bottom of the fuselage (Fig. 4) was determined optically. The SPR technique is based on a 3-dimensional reconstruction of visible marker locations by using stereo camera images. The accuracy of marker position recognition depends on the resolution and angular set-up of the cameras and on the marker shape and size. For the conditions of the HART II test measurement the theoretical resolution is $0.4mm$ in $x-$, $y-$ and $z-$direction. A more detailed description of the method is presented in [6] and [9]. The cameras were triggered to the rotor azimuth and 50, sometimes 100 repeats per position were recorded. The data contain the low frequency motion of the model as spatial scatter. This motion is increasing with blade radial position since the air loads generating the blade motion are also subject to vary according to the model motion.

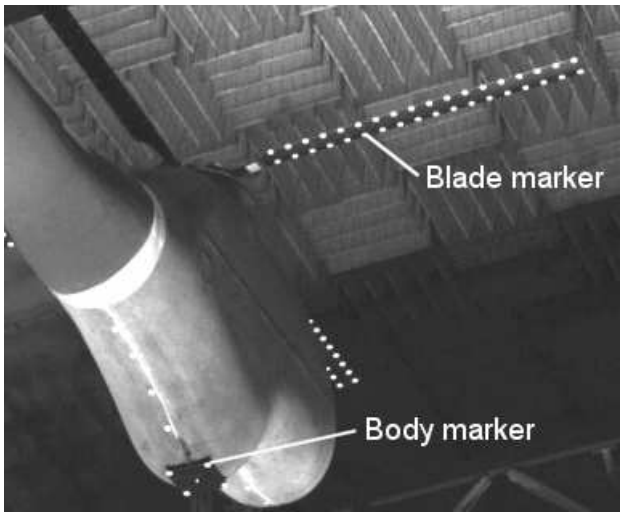

Figure 4: SPR image of the downsream right camera at $90deg$

To get smooth data with reduced errors and eliminated vibrations it is necessary to determine averages of the coordinates. To average the marker coordinates a simple mean value for each correctly recognized marker of all repeats was computed. In Fig. 5(a) and Fig. 5(b) an example is shown for two different markers at the $90deg$ azimuth position of blade 1 of the base line case.

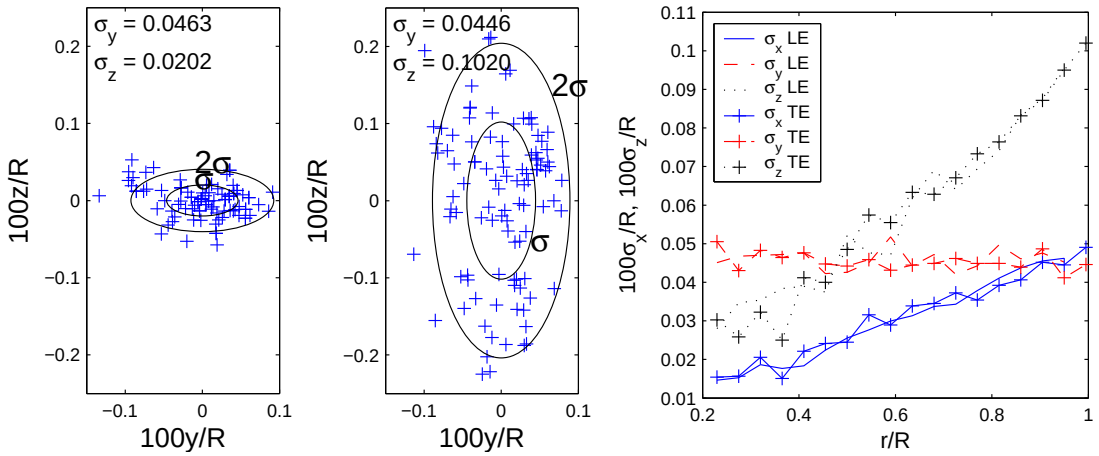

(a) Body marker

(b) Blade tip marker (trailing edge) at 99%R

(c) Standard deviation in $x-$ and $z-$direction for leading and trailing edge markers

Figure 5: Scatter of body and blade markers at $90deg$ BL

At the location of the body marker (left figure) the scattering is by about $4mm$ in $y-$direction (lateral) and $2mm$ in $z-$direction (vertical). Comparing this with the scattering at the blade tip the vertical scatter

is increased to up to $9mm$, caused by varying air loads from one revolution to the other, while in the horizontal direction no change in scattering is visible (the blade is stiff radially).

In Fig. 5(c) the standard deviations σ in all directions are shown for both the leading and trailing edge markers depending on the blade radius. It clearly can be seen that there is no dependence of the $y-$scatter on the radius due to large radial stiffness of the blade, it is nearly constant and only influenced by the low elasticity of the wind tunnel sting. The $x-$ and $z-$scatter increase with the blade radial location because of the changing airloads, the blade elasticity in flap, and model motion.

The analysis of SPR results requires some post-processing since the data contain only positions of the markers along leading and trailing edge in space, i.e. in the wind tunnel coordinate system. The goals are flap, lead-lag and torsion displacements of the quarter chord line in the shaft coordinate system with origin in the center of the rotor hub. To obtain these results, the position of the hub center must be known and several procedures have to be applied (Fig. 6).

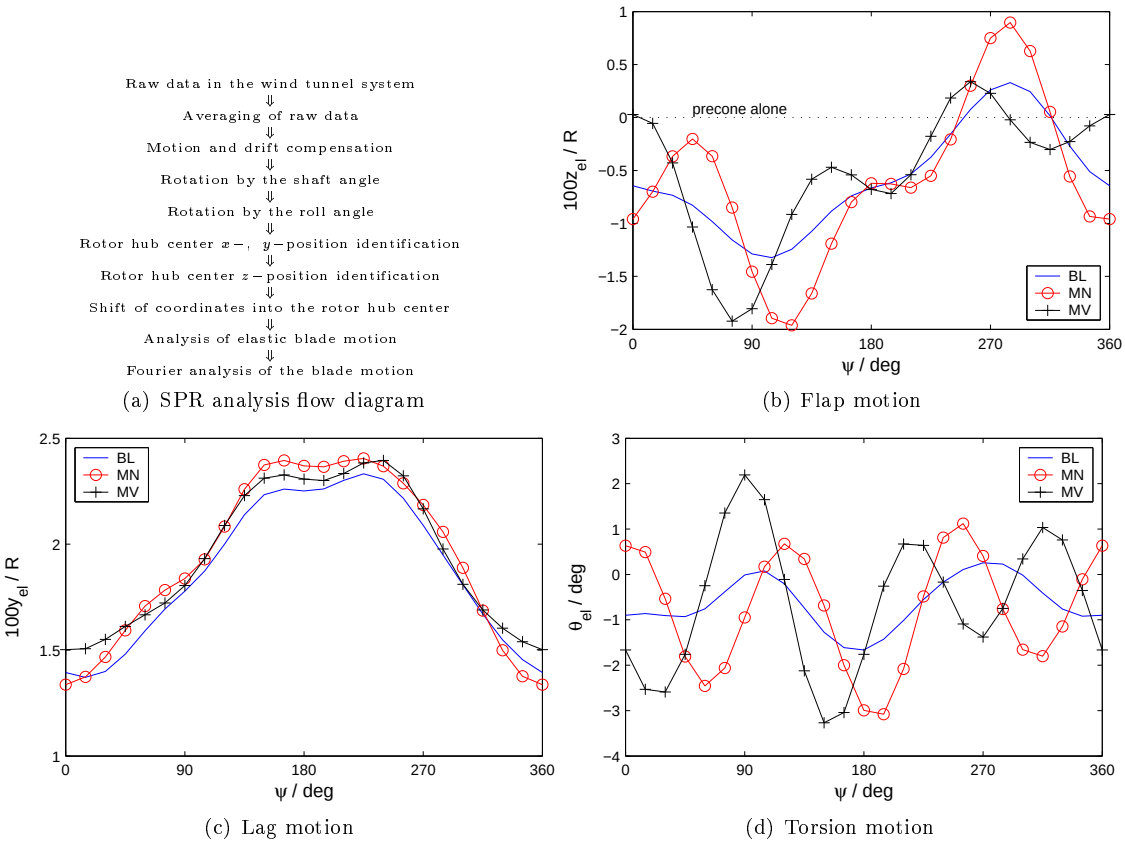

(a) SPR analysis flow diagram

(b) Flap motion

(c) Lag motion

(d) Torsion motion

Figure 6: Post-processing procedure and results of SPR: Elastic tip motion depending on rotor azimuth for HHC-sweep, blade 1 (measurement accuracy: $100\Delta z/R = 0.02$ in flap and lag; $\Delta\theta = 0.5deg$; airfoil thickness: $100\Delta z/R = 0.726$)

During the measurements dynamic marker position displacements due to low frequency motions of the wind tunnel sting, vibrations of the rotor model and of the sting support were present. Also a drift in sting yaw led to a lateral drift of the entire model. To correct this drift (up to $10mm$ within the 23 azimuth locations) the drift of the body markers is used. The difference between the mean value at one azimuth to the mean value from all azimuths define the body drift. Based on this drift all blade marker coordinates were modified. The results have shown that the body marker positions differ in measurements of the advancing and retreating side. That is why the drift compensation was made separately for each side.

After drift compensation the data in DNW coordinate system have to be transformed into the rotor hub coordinate system to obtain the parameters of blade motion. This is done by rotating the coordinates by the rotor shaft angle and the rotor roll angle into a coordinate system parallel to the rotor shaft and transformation (shifting) of all marker coordinates into the rotor hub center coordinate system. Then the elastic blade motion can be extracted and a smothed distribution of the three components flap, lead lag and torsion can be obtained by means of a Fourier representaion (see Fig. 6(a)). In the calibration data,

which were taken innon-rotating condition, it was found that the model has had a small roll angle and a shaft angle that were non-zero. The roll angle was measured to 0.145deg instead of zero. Due to support elasticity the rotor shaft angle has had an offset of about 0.15 deg that was also taken into account in the further analysis.

Unfortunately the rotor hub center could not directly be measured, since the SPR cameras were located below the model. A suitable method for hub center identification was found in the circular regression of single blade markers (compute best fit circles of the positions from one revolution to get the $x-y-$center point). There is one circle center point obtained for each blade marker which resulted in a scattering of about $1.0mm$ in $x-$direction and $1.1mm$ in $y-$direction in all configurations. When the hub center positions calculated by using different blades are compared, the maximum deviation is about $0.8mm$ in x-direction and only $0.2mm$ in $y-$direction which is in the order of the SPR measurement accuracy.

After the hub center coordinates in $x-$ and $y-$direction are found, the position in $z-$direction of the rotor hub center is in demand. At first the coordinate system must be shifted into the hub center found so far. This means a transformation of all blade and body markers into a coordinate system with the origin in the rotor hub $x-$, $y-$center point, while the origin in z is yet anywhere on the shaft axis. To identify the rotor hub $z-$coordinate, a polynomial of fourth order with an additionally constraint is used. It is assumed that the gradient dz/dr at the position where the blade is fixed is equal to the precone angle of $2.5deg$ as a boundary condition. Finally the coordinats can be shifted into the rotor hub center coordinate system and the blade motion parameters can be computed.

The elastic blade flap deflection z_{el} (positive up) is computed by the distance between the quarter chord line and a straight line defined by the pre-cone angle. Therefore approximately the distance of the quarter chord line $z-$position to the pre-cone line at defined radial positions is used. The elastic blade lead-lag deflection y_{el} is given by the distance between the radial position of the quarter chord line and a straight line defined by the current azimuth position of the blade (lag positive). The pure elastic pitch deformation θ_{el} (positive nose up) can be calculated by the distance of the $z-$coordinate of the front and rear blade marker after subtracting the associated pitch control angle, the pre-twist angle and the pitch offset in $z-$direction due to the different distance of the front and rear blade markers to the quarter chord line.

Fig. 6(b), Fig. 6(c) and Fig. 6(d) show the comparison of the elastic flap, lead-lag and torsion motion of the rotor blade tip for the reference blade depending on azimuth for the configurations with higher harmonic control and the base line case at the blade position $r/R = 99\%$. When $3/rev$ HHC is applied (cases MN and MV), a $3/rev$ flapping dominates the figure (Fig. 6(b)) as expected. We find local amplitudes of up to $0.6\%R$ off the BL position at the blade tip in the minimum noise case. The results of the blade lag motion show nearly identical values with $1/rev$ amplitudes of about $0.5\%R$ independent of the higher harmonic control (Fig. 6(c)). With $3/rev$ HHC a strong $3/rev$ torsion is the response which was expected due to the natural frequency in torsion at $3.6/rev$ of this rotor. The local amplitudes in torsion are up to $1.5deg$ off the BL values in the minimum noise case and up to $2.5deg$ in the minimum vibration case.

4 Tip vortex position and flow field analysis

The PIV measurements were triggered to the rotor reference blade azimuth such to obtain images of the tip vortex from the same reference blade and the same observation area in space and in time for averaging purposes and statistical analysis.

As an example, the tip vortex of the MV case created at $y = 0.7R$ on the advancing side at about $\psi = 135deg$ is created by a local download with a pretty sharp gradient of the blade circulation towards the tip. This vortex is nicely shaped right from the beginning and based on the analysis of 100 repeat measurements these have a vertical scatter of $0.068\%R$ and a horizontal scatter of $0.058\%R$ in the observation area when the vortex is just created, Fig. 7(a). The vertical scatter represents the variation in the blade tip position as given by means of SPR results shown in Fig. 5, while the horizontal scatter represents the radial position on the blade where the vortex is generated, which is biased also by body motion in this direction. More than one rotor revolution later the scatter has significantly grown in both directions due to the so called vortex wander effect [3, 7] and due to close encounters with passing blades (BVI), Fig. 7(b). It can also be seen that the distribution of vortex positions is rather homogenous within the range of σ instead of being clustered with higher density around the mean value and thus does not represent a Gaussian normal distribution. The growth trend is progressive as can be seen in both the horizontal and vertical scatter components in Fig. 7(c) and Fig. 7(d), respectively. The initial scatter as

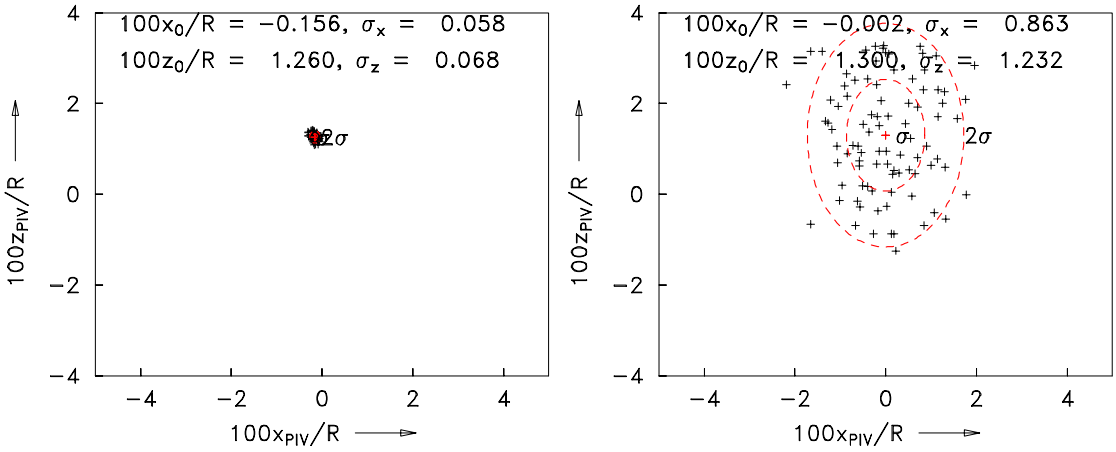

(a) $\psi_V = 5.5deg$, Pos. 17a (b) $\psi_V = 425.5deg$, Pos. 22

a, b: scatter of vortex centre position at different vortex age, MV, $y/R = 0.7$

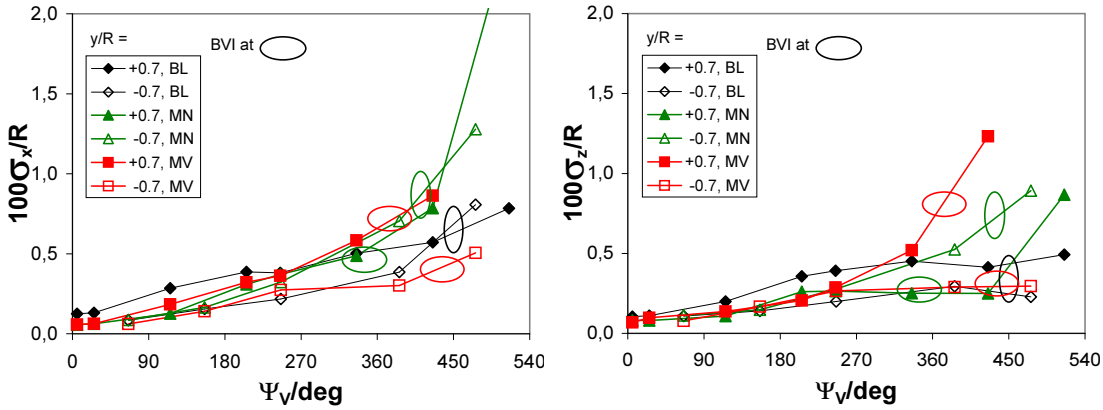

(c) Standard deviation of vortex horizontal position (d) Standard deviation of vortex vertical position

Figure 7: Tip vortex position scatter (observation area coordinates).

well as the growth of scatter is found to be similar for all three cases and independent of applying active control or not.

Two methods of averaging have now been applied: the simple averaging (SA), and the conditional averaging (CA) method. The SA is suspected to lead to increasingly erroneous results in terms of vortex properties like core radius, swirl velocity and vorticity when the vortex position scatter is growing. To circumvent these problems, a conditional averaging must be applied as described in [7]. The SA needs no further explanations since it applies the arithmetic averaging to the 100 data sets on every individual vector of the field. The CA method first identifies all individual vortex centre coordinates, then shifts all individual vortices with their centre to the average centre position (= alignment of the centres) and finally averages all individual measurements for each vector. Due to the shifts, the vectors at the border of the observation area are not covered by each data set such that the resulting field is based on a non-homogenous number of samples. However, this does not affect the vortex analysis as long as the vortex is close to the image centre, which is the case in virtually all measurements. The flow chart of post-processing the individual vector maps is illustrated in Fig. 8. Most options can be switched on or off using control parameters, and an automatic processing is possible in most of the data available. Manual control however, is necessary in tricky cases, for example, when a blade has passed very close to the vortex and a decision must be made which of the vortices to select for averaging.

The effect of averaging methodology on the resulting velocity field is shown next at the example for a vortex of the MN case on the advancing side. Due to active control this vortex is generated by a higher blade loading at the point of vortex creation, compared to the BL case. In Fig. 9(a) and Fig. 9(b) the first individual measurements at a vortex age of $\psi_V = 5.5deg$ and $335.5deg$, respectively, are shown for comparision with the averaging methods. In-plane velocity components are shown as vectors and the cross-flow velocity is color-coded. They are noisy due to flow turbulence and measurement uncertainty. For the very young vortex the differences between the averaging methods appear negligible in both the

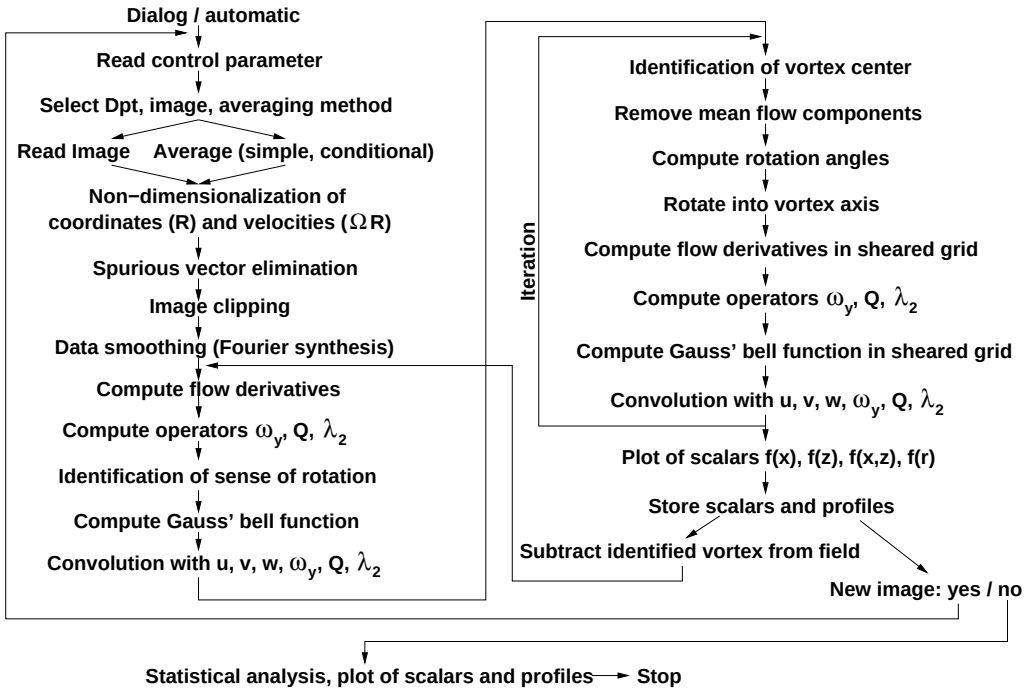

Figure 8: Post-processing flow diagram for 3C-PIV data.

in-plane velocity components and the cross-flow velocity, see Fig. 9(c) and Fig. 9(e). This means the position scatter is small enough compared to the dimensions of the tip vortex and the shear layer behind the rotor blade. The core radius, indicated by the circle, is essentially the same in both averaging methods, and the measurement noise is also successfully suppressed by both methods. For the old vortex, however, the differences become visible in all parameters. The axial velocity in the vortex center is much more pronounced and the core radius is significantly smaller in the result of the CA method, Fig. 9(f), compared to the SA method in Fig. 9(d). In this case the position scatter is significantly exceeding the dimensions of the flow structure to be observed and thus CA must be applied.

This result is further demonstrated at the velocity profiles in a horizontal cut through the vortex centre for the same data sets. For the young vortex in Fig. 10(a) and the old vortex in Fig. 10(b) the result of the SA and the CA method are compared with each other and with the first 5 of the 100 individual measurements. Due to the small spatial scatter the young vortex allows the application of the SA method, but this is obsolete for the old vortex with large scatter where the SA method leads to artificially large core radii and smaller swirl velocities than any of the individuals. In contrast, the CA method retains both the core radii and the swirl velocity. These spatial distributions of the swirl velocity are an analogon to the principle shown in Fig. 1, and since the vortex centre is scattered in both directions this effect is visible in both velocity profiles $u(z)$ and $w(x)$. Thus, a two-dimensional correction has to be applied, which is represented by the CA method.

It must be recognized that this spatial scatter in two dimensions will be reflected two-fold in the blade aerodynamic loading and consequently in the acoustic time histories. First, the vertical vortex position scatter will be visible in a scatter of BVI-related pressure peaks (and the associated $C_n M^2$) and thus a scatter of BVI intensity, which can be handled using standard averaging procedures. In contrast, the horizontal vortex position scatter will translate into azimuthal variations of where this BVI happens. In this case, a standard averaging procedure artificially smoothes the BVI signature and again a derivative of the CA method must be applied.

5 Blade pressure and section loading time histories

During the HART II test, blade pressure data were recorded by means of absolute pressure sensors with a data rate of $2048/rev$, triggered to the rotor azimuth. 80 continuous revolutions were taken such that low frequency oscillations of the model are directly visible in these data. The vortex wander addressed in the last section leads to a twofold effect: First, the vertical position scatter translates into a scatter in the magnitude of blade-vortex interaction (BVI) strength due to different blade-vortex miss-distances

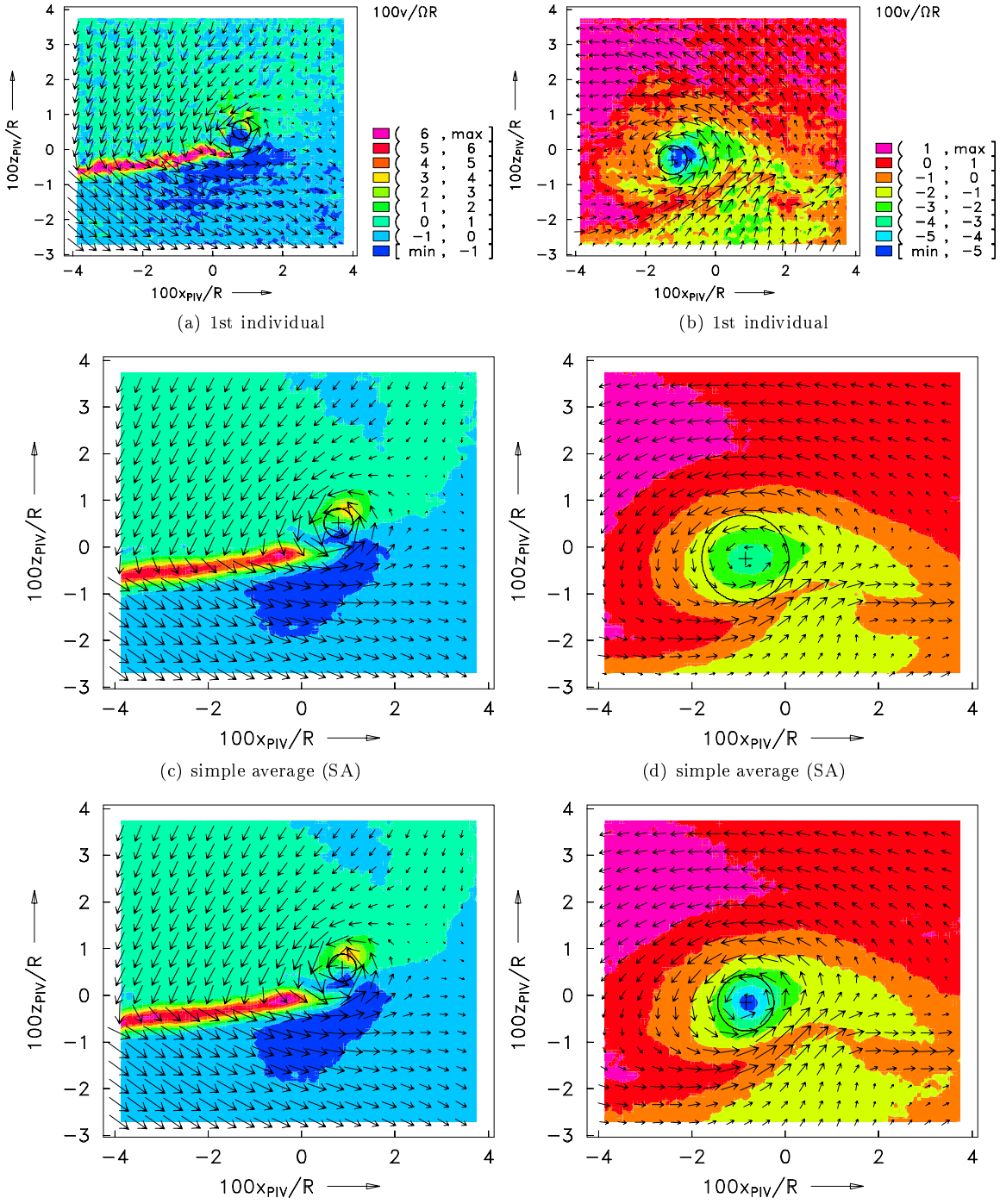

(a) 1st individual

(b) 1st individual

(c) simple average (SA)

(d) simple average (SA)

(e) conditional average (CA)

(f) conditional average (CA)

a, c, e: Pos. 17a, $\psi_V = 5.5deg$ b, d, f: Pos. 22, $\psi_V = 425.5deg$

Vectors: in-plane velocities u and w; color-coded: cross-flow velocity v. Mean values are subtracted, observation area coordinates. The core radius is indicated by the circle, every 5th vector shown.

Figure 9: Effect of averaging method on the velocity field, MN, $y/R = 0.7$.

revolution by revolution. Second, the horizontal position scatter of the vortex translates into an azimuth (or time) jitter for blade pressure time histories, without magnitude effect. All these effects combine to produce both a magnitude scatter and a time jitter of these BVI-events in each revolution. A simple averaging would lead to artificial smoothing of such BVI-events (as is the case for PIV analysis), while the conditional averaging method applied to the time histories is able to completely eliminate the time jitter before averaging only the magnitude scatter.

The computations were made using the force coefficient normal to the chord center line, $C_n M^2$, for

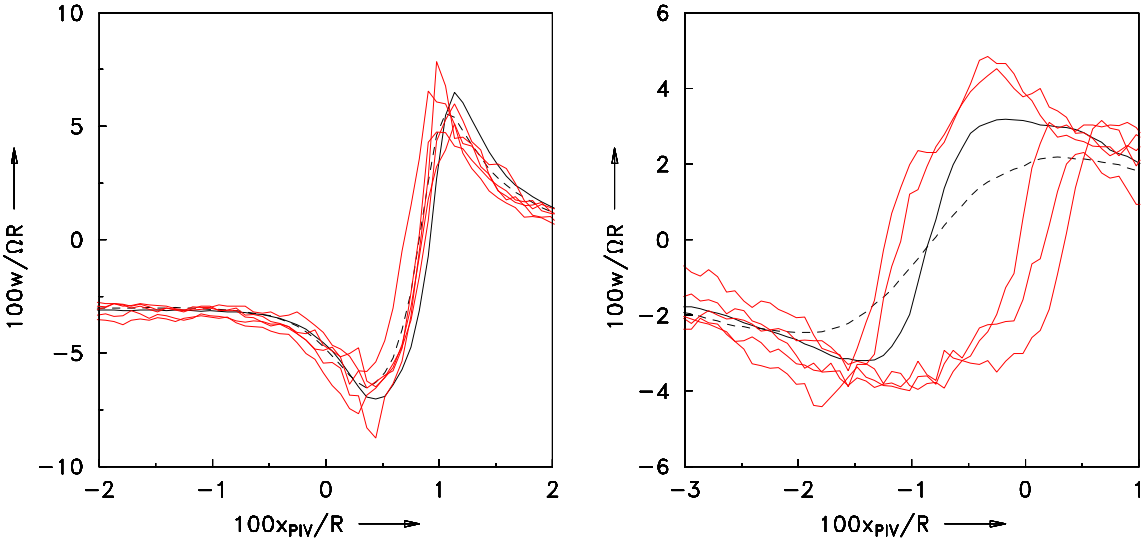

(a) $\psi_V = 5.5deg$, Pos. 17a (b) $\psi_V = 425.5deg$, Pos. 22

Black solid: CA, dashed: SA; red: 5 individual; mean values are subtracted, observation area coordinates.

Figure 10: Effect of averaging method on the swirl velocity, MN, $y/R = 0.7$.

the three operational conditions BL, MN and MV. To get a physically correct averaged blade pressure time history of all 80 consecutively measured rotor revolutions with respect to BVI phenomena (which are in the frequency range of about $20 - 200/rev$), it is not enough to simple average the C_nM^2 values at each sample (for rotor loading purposes, which are covering the frequency range of about $0 - 6/rev$, simple averaging is by far sufficient). Further, a more detailed view on the raw data is needed to get the correct time history by conditional averaging. For calculation of the normal force coefficient C_nM^2 the pressure time histories at a radius of $r/R = 0.87$ of 11 Kulite sensors on the upper side and 6 on the lower side of the reference blade were available. The chord-wise distribution is shown in Fig. 11.

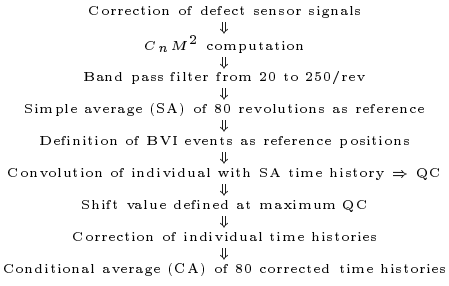

(a) Pressure analysis flow chart

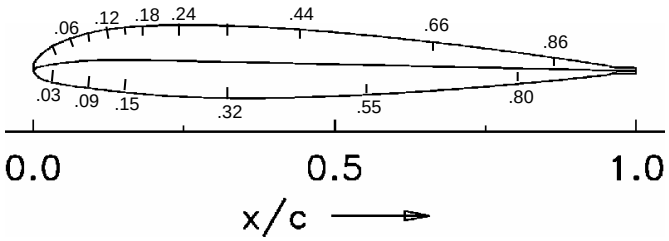

(b) Airfoil section

Figure 11: Chord wise blade pressure sensor distribution as used in HART II, $r/R = 0.87$

In [3] aliasing problems are described for distinct frequencies of specific multiples of the sampling rate. Isolated spikes were found at $128/rev$, $256/rev$, $512/rev$, and $768/rev$ with about $20dB$ magnitude more than the signal should exhibit. An explanation of this problem could be very high frequency signals in some data acquisition cables that lead to disturbed pressure signals. To remove the disturbed frequencies a harmonic analysis of the according pressure signal is made for each frequency which has to be corrected to get the sine and cosine coefficients. Thereafter, by using a harmonic synthesis, all parts of these frequencies are added together and finally subtracted from the original time history.

To fit all individual time histories together for corrected amplitude and phase width of the averaged time history a couple of procedures are needed (Fig. 11(a)). The main problems are the different locations of the centre of a BVI-event (=its time scatter) and thus the scatter in location of the associated minimum and maximum peaks (beginning and ending of a BVI-event) which is caused by fluctuations in rotational speed and varying vortex locations due to vortex wander when passing the blade. The typical BVI signature at the advancing side has a steep increasing flank caused by the swirl velocity field of the vortex

passing the blade, which is downwards, when the blade is approaching the vortex. After passing the vortex centre the swirl velocity is directed upwards which produces an increasing C_nM^2. At the retreating side, the BVI signature is the other way round since the blade approaches the vortex from the opposite side. A steep decreasing flank is present while passing the vortex centre. The azimuth locations where BVI takes place are strongly dependent on the operating condition and can best be visualized by the high frequency content of the blade leading edge pressure along radius and azimuth. For the cases investigated here, they are mainly between $\psi = 10deg$ and $\psi = 90deg$ at the advancing side and between $\psi = 270deg$ and $\psi = 350deg$ at the retreating side.

To find the BVI-events where a correction of the time phase is needed a band pass filtering between $20/rev$ and $250/rev$ is done for all individual C_nM^2 time histories in order to eliminate the large low-frequency content and thus to leave over only the interesting frequency range of BVI-events. Therein, the signature of one BVI-event time history is characterized by a decreasing flank followed by a steep increasing flank and again a decreasing flank at the advancing side and the other way round at the retreating side due to the physics of vortex interactions as described above. The simple averaged time history already provides the correct location of BVI-events, but neither the correct magnitude nor the correct azimuthal extension to the right and left of the event itself. It is used as reference for a convolution with the individual time histories. The vortex centre of a BVI location is defined using the simple averaged data where $C_nM^2 = 0$. For each BVI-event there is one convolution function ($= CF$), which is defined by the band-pass filtered values of the simple averaged time history between the according starting and ending point of a BVI-event. For the convolution itself, the region of interest of each individual C_nM^2 time history is multiplied with the CF to get a quality criteria ($= QC$). The starting point is shifted from -15 samples to $+15$ samples ($\pm 2.6deg$ of azimuth), which covers the maximum shift of events observed. The resulting QC (Eq. 4) is a measure for the coincidence between both the individual and the simple averaged time histories.

$$QC(j) = \sum_{j=-15}^{+15} \left(\sum_{i=BVIstart}^{BVIend} CF(i) \cdot C_nM^2(i+j) \right) \tag{4}$$

This procedure, applied to all BVI-events, leads to individual values of shift for the advancing and retreating side according to the number of BVI-events. In general, the shift values obtained differ by about 5.5 samples, which corresponds to about $\psi = 1deg$ of rotor azimuth. It was found, that there is no dependency between the values of shift of the advancing and the retreating side. For one individual rotor revolution the shifts of advancing and retreating side are completely different and no systematic behaviour is visible in all three flight cases. On the other hand the shift is nearly constant within each side, thus, the phase shift correction has to be applied independently on the advancing and retreating side. When all shifts of each BVI-event are known, the phase correction can be done. The correction is made by the assumption that the reference location is at an integer sample number at the position where the steep increasing flank (advancing side) or steep decreasing flank (retreating side) has a value near $C_nM^2 = 0$. To displace the C_nM^2 values in time a linear stretching or compression (depending on positive or negative shift) between two reference points is used. Since the required shifts found have real indeces an interpolation is necessary to get finally the new C_nM^2 values depending on an integer time index (which is needed for averaging).

All individual time histories are corrected (shifted and interpolated) that way and a new mean value can be computed. In Fig. 12 all 80 C_nM^2 time histories are plotted for the retreating side of the BL case before (Fig. 12(a)) and after (Fig. 12(b)) the time phase correction. After correction, the location of the steep decreasing flank is nearly identical for all time histories and the maximum and minimum peaks are at the same locations as well. Finally, the average time history can be computed, which is now called the conditionally averaged time history.

For comparison between the simple averaged and conditional averaged time histories, the peak-to-peak amplitudes and peak-to-peak time differences for the selected BVI-events were investigated. Changes could be found with respect to the peak-to-peak amplitudes between the conditional average and the simple average, which led always to increases of up to $C_nM^2 = +3.6 * 10^{-3}$ or $+8.4\%$ around the BVI-events. However, these values are not so much expressive, since the magnitude of the amplitudes are very different. The peak-to-peak azimuthal distances between the C_nM^2 extreme values of the conditional averaged C_nM^2 values compared to the peak-to-peak azimuth width of the simple averaged values show decreases of up to -1.8 samples ($-0.32deg$). The percentage differences are between $+0.3\%$ up to -7.8% (see also Fig. 13(a)).

In any flight case, the conditional average has larger C_nM^2 amplitudes at the BVI-events, while the peak-to-peak azimuth distance between the extreme values of the BVI-event mostly is smaller compared

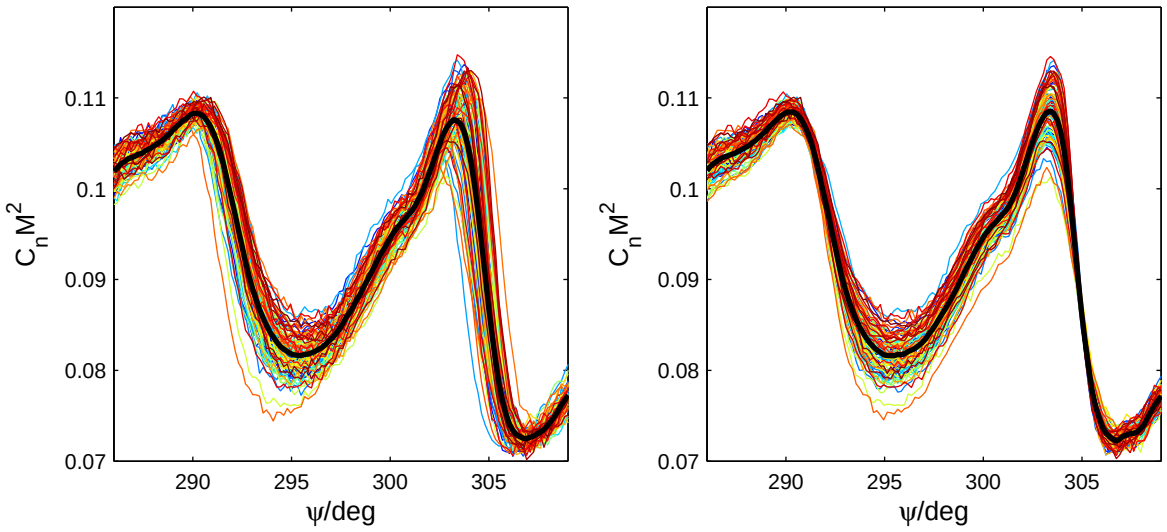

(a) before correction

(b) after correction

Figure 12: 80 individual C_nM^2 time histories before (a) and after (b) time jitter correction (BL, data band pass filtered from 20-250/rev)

to the simple averaged time histories. Although the differences between simple and conditionally averaged data may appear as not important, the physics of rotor BVI noise are based on time derivative of C_nM^2, which significantly exaggerates the differences (Fig. 13(b)).

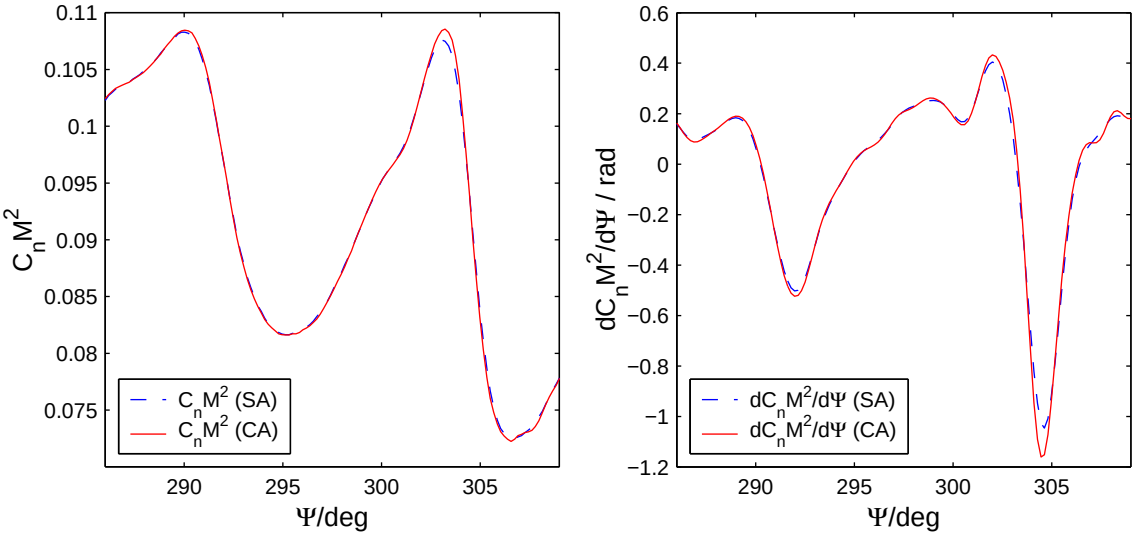

(a) Normal force coefficient C_nM^2

(b) Time derivative of C_nM^2

Figure 13: Comparison of normal force coefficient C_nM^2 and its time derivative for simple and conditional average (BL, data band pass filtered from 20-250/rev), $r/R = 0.87$

6 Microphone time histories

Since blade pressure time histories (Sect. 5) are the source of noise generation all effects of time jitter and magnitude scatter are also found in microphone pressure time history data in the same manner. For investigations of the effect of conditional averaging on microphone signals the unfiltered raw data of the base line case (BL) of microphone 11 at the advancing side and microphone 4 at the retreating side are used. For each microphone location data were stored for 100 consecutive revolutions with an increment of 2048 samples per revolution, units are Pascal [Pa]. The locations of the microphones relativ to the

rotor hub center are $x = 2.0m$, $y = -1.34m$ for microphone 4 and $x = 0.01m$, $y = 1.81m$ for microphone 11. These locations were chosen because they are very close to the maximum peaks of the noise contour (Fig. 14), one at the advancing and one at the retreating side.

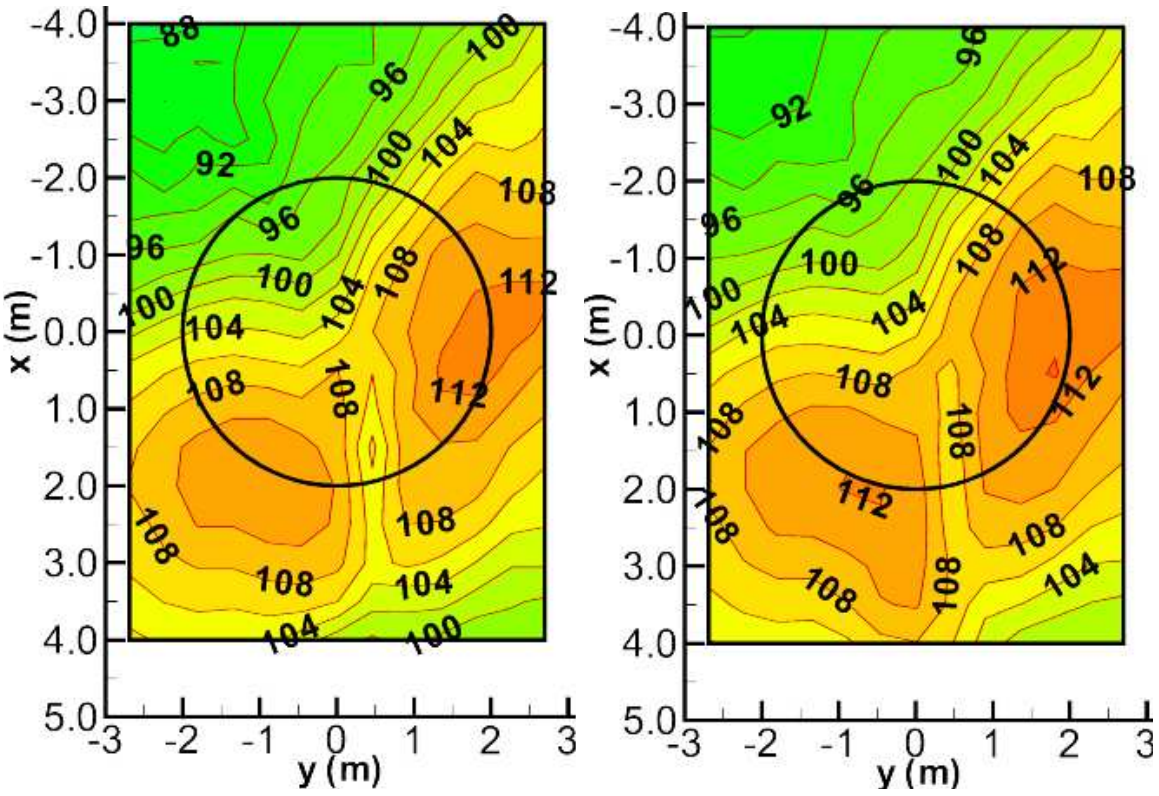

(a) Simple average

(b) Spectra average

Figure 14: Noise directivity contour base line case (BVI-SPL)

The spectrum of the simple averaged microphone time histories then leads to significantly lower noise levels than the individual spectra, since the peaks of pressure are smoothed unrealistically large. To cover the problems associated with this time jitter, in the past the average of all individual spectra was used as being representative for the averaged noise spectrum. Each of the microphone pressure time histories show four typical events within one rotor revolution. These events are caused by the BVI-events of the rotor blades and since the model rotor is four-bladed there are four main events at each microphone per revolution. As mentioned in Sect. 5 the simple averaged time history already provides the correct location of BVI-events, but not the correct magnitude nor the correct azimuthal width of the event itself. Again, a convolution is made and the best convolution function to be compared to a single time history is assumed to be the simple averaged time history of all the 100 revolutions. It is also used to set the reference points respectively the reference azimuth locations. For the microphone data no filtering is necessary, since there are only pressure oscillations around the static pressure. Here the reference points were chosen to be on the steep increasing flank at the zero crossing between the minimum and the following positive maximum value of a BVI-event.

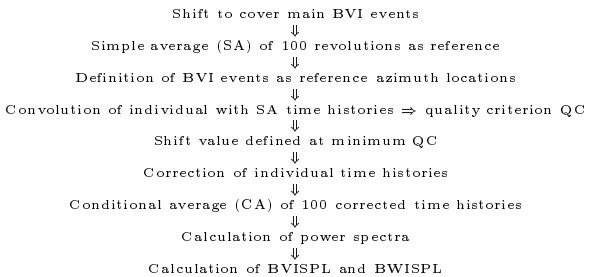

Figure 15: Post-processing flow diagramm for microphone data

For finding the individual shifts between each individual time history and the simple averaged time history at the main BVI-events again a convolution is made in a range of ±32 samples around the according reference point (RP) to have best coincidence. By means of the least error squares method a quality criteria $QC(j)$ is computed where CF is the convolution function extracted from the simple averaged time history. The convolution is made in a range of ±16 samples, which covers the maximum shift of events observed (Eq. 5). At the shift value where the individual time history best fits with the CF the QC at this sample is minimal. To find the minimum QC, a best fit polynomial of 2^{nd} order is computed by means of regression analysis using five values around the minimum.

$$QC(j) = \sum_{j=-16}^{+16} \left(\sum_{i=RP-32}^{RP+32} (CF(i) - p(i+j))^2 \right) \tag{5}$$

Since four main events are present within one rotor revolution, this procedure has to be applied to all of them. Finally we get four individual shift values for each microphone time history. All BVI-events have nearly the same shift values within one revolution. As in blade pressure data the shift values differ by about ±5.5 samples in maximum, which corresponds to about $\psi = 1deg$ of rotor azimuth. Comparing this magnitude to the shift results found in the C_nM^2 analysis in Sect. 5 a similar behaviour is found. The fluctuations in rotational speed and varying vortex locations, which lead to these shifts, are present at the blades as location of noise source as well as at the microphone positions. Finally the adjustment of the individual time histories is done according to the procedure (by linear stretching/compression) mentioned in Sect. 5 and a new average can be computed - now called the conditional average. In Fig. 15 the post-processing flow chart for microphone data is shown and Fig. 16 shows the comparison of the raw data and the corrected microphone pressure time histories.

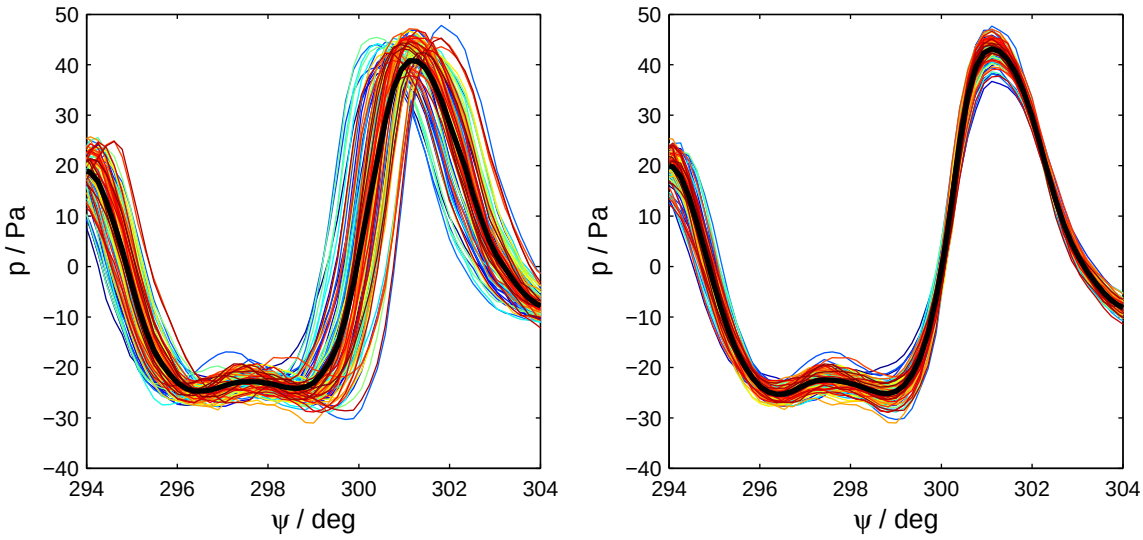

(a) before correction

(b) after correction

Figure 16: 100 individual pressure time histories before (a) and after (b) time jitter correction (Microphone 4)

The comparison of simple and conditional averages leads to increases in peak-to-peak amplitudes between +4.4% and +6.5% for both microphones while the peak-to-peak azimuth differences always decrease by about −1% to −10%. This leads to remarkable changes of the gradients $dp/d\psi$ at the main BVI-events. The difference of the gradients of microphone 4 (+15.4% to +34.2%) is about twice as large as the differences found in the microphone 11 results (+8% to +13.4%).

In helicopter acoustics the sound pressure level or power spectrum of microphone data is important for noise estimations. There are two main frequency bands of interest. With respect to the BVI-noise the relevant frequency range is between the 6^{th} and 40^{th} blade passage frequency (bpf) which is $24/rev$ to $160/rev$ for a four-bladed rotor, for the BWI-noise (Blade Wake Interaction) the range between 40^{th} and 100^{th} bpf ($160/rev$ to $400/rev$ for a four-bladed rotor). In these two frequency ranges the according sound pressure levels (SPL in decibel) can be computed as logarithm of the square root of the sum of pressure amplitudes, divided by a reference pressure p_{ref} (defined by the ability of the human ear):

$$BVISPL = 20 \cdot log\left(\sqrt{\sum_{i=24}^{160} \Delta p(i)} \cdot \frac{1}{p_{ref}}\right) \qquad (p_{ref} = 2 \cdot 10^5 Pa) \tag{6}$$

At first the power spectra (SPL) are calculated by means of a FFT for both the simple and conditionally averaged time histories (Fig. 17(a)). Additionally the spectra average is plotted, which is the average of the individual spectra from each of the 100 time histories. The conditional average spectrum, compared to the simple average spectrum, shows higher amplitudes in the lower frequency ranges as expected and thus is closer to the average spectrum. To have a better relation between the three spectra only the peaks at multiples of the blade passage frequencies are selected and plotted in the BVI-SPL frequency range as the upper envelope in Fig. 17(a). It clearly can be seen that the conditional average is very close to the spectra average and thus more capable to get accurate BVI-SPL calculations.

Finally the BVI-SPL results can be compared (Fig. 17(b)). The values scatter by about 2 to 2.5dB for both microphone data. While for microphone 4 the BVI-SPL of the simple averaged data is 0.38dB lower than the spectra average BVI-SPL (111.66dB), the BVI-SPL of the newly computed conditional average is only 0.1dB lower. The same tendency could be found in the microphone 11 results , where the difference to the spectra average BVI-SPL (113.56dB) now is reduced from 0.64dB (SA) to 0.18dB (CA). Even the blade wake interaction (BWI) noise spectrum is much better computed based on the conditional averaged pressure time histories, compared to simple averaging.

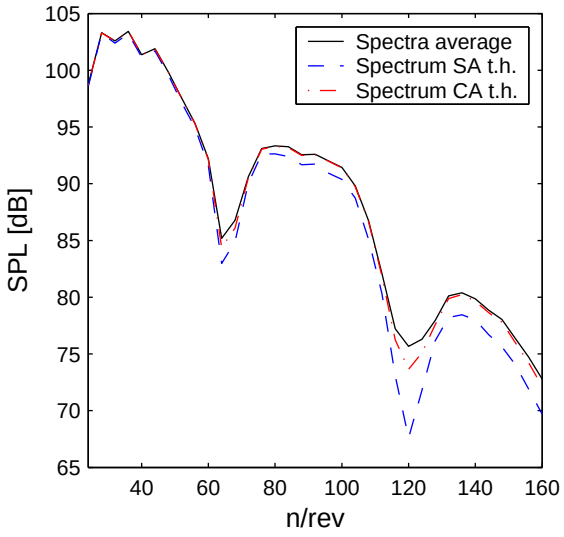

(a) Upper envelope of the power spectra of microphone 4, only blade harmonics in BVI-SPL range

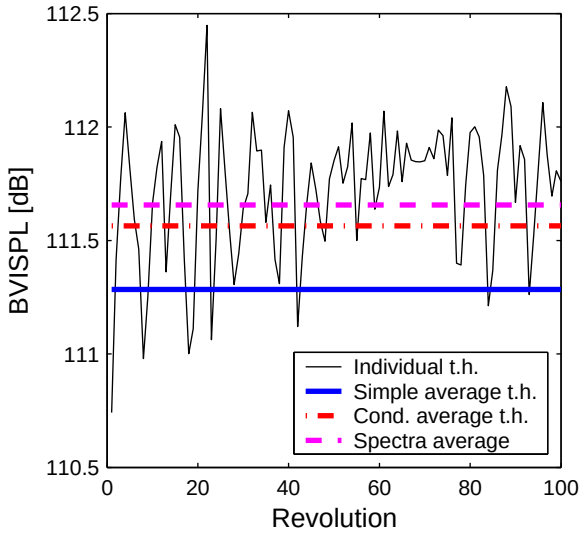

(b) BVI-SPL of microphone 4

Figure 17: Results of conditional averaging wrt sound pressure level (Microphone 4)

7 Conclusions

The physics of time jitter and its effects on simple averaged time history data are demonstrated and clarified in this paper. The method of conditional averaging provides a good means to eliminate spatial scatter effects required for the analysis of flow field vector maps, and also to eliminate the time jitter of BVI events in the individual time histories. This is especially valid for highly sensitive data like microphone pressure time histories. Consequently, conditionally averaging is intended to be mandatory for the generation of reliable averaged time histories of blade (and microphone) pressure or flow fields (in order to retain the high frequency effects like BVI or small structures like tip vortices in their individual magnitude) for code validation purposes.

References

[1] B.G. van der Wall, C.L. Burley, Y.H. Yu, K. Pengel, P. Beaumier, *The HART II Test - Measurement of Helicopter Rotor Wakes,* Aerospace Science and Technology, Vol. 8, No. 4, pp. 273-284, 2004

[2] B.G. van der Wall, *2nd HHC Aeroacoustic Rotor Test (HART II) Part I: Test Documentation -,* DLR-IB 111-2003/31, 2003

[3] B.G. van der Wall, C.L. Burley, *2nd HHC Aeroacoustic Rotor Test (HART II) Part II: Representative Results -,* DLR-IB 111-2005/03, 2005

[4] *HART II international workshop web site,* ftp://HART-II@ftp.dlr.de

[5] T.F. Brooks, *Effect of Signal Jitter on the Spectrum of Rotor Impulsive Noise,* Vertica, Vol. 12, No. 3, pp. 257-265, 1988

[6] O. Schneider, *Analysis of SPR measurements from HART II,* Aerospace Science and Technology, Vol. 9, No. 5, pp. 409-420, 2005

[7] B.G. van der Wall, H. Richard, *Analysis methodology for 3C-PIV data of rotary wing vortices,* Experiments in Fluids, Vol. 40, No. 5, pp. 789-812, 2006

[8] W.R. Splettstößer, R. Kube, U. Seelhorst, W. Wagner, A. Boutier, F. Micheli, E. Mercker, K. Pengel, *Key Results from a Higher Harmonic Control Aeroacoustic Rotor Test (HART) in the German-Dutch Wind Tunnel,* 21^{st} European Rotorcraft Forum, Saint-Petersburg, Russia, 1995

[9] Pengel, K., Müller, R., van der Wall, B.G., *Stereo Pattern Recognition - the Technique for Reliable Rotor Blade Deformation and Twist Measurement,* AHS International Meeting on Advanced Rotorcraft Technology and Life Saving Activities, Utsunomiya, Tochigi, Japan, 2002

[10] Raffel, M., Richard, H., Schneider, G., Klinge, F., Ehrenfried, F., Pengel, K., Feenstra, G., *Recording and Evaluation Methods of PIV Investigation on a Helicopter Rotor Model,* 11^{th} International Symposium on Laser Applications to Fluid Mechanics, Lissabon, Portugal, 2002